Chapter 2
Radiation Damage in Silicon Detector Devices

The intent of this chapter is to introduce the radiation effects and give a general understanding of radiation damage – its mechanism, microscopic and macroscopic effects. The very basics of radiation damage are presented in [219] (Description of the so-called "Hamburg Model") and [356, 357], recent studies on fully segmented sensors on a large sample can be found in [79] and [80]. The three main effects (bulk and surface defects) introduced by radiation are

- displacement of atoms from their positions in the lattice (bulk)
- transient and long-term ionisation in insulator layers (surface)
- formation of interface defects (surface)

2.1 Bulk Damage

Detectors at the LHC and also already at the TEVATRON operate at high particle fluxes, necessary to achieve a large statistical sample on particle collisions, to understand physics of the events in a hadron collider environment. To understand the depletion voltage, leakage current or trapping of an irradiated sensor the following mechanisms have to be taken into account:

1. the damage to the lattice created by traversing particles
2. the following diffusion[1] processes – annealing

The following sections describe the microscopic and macroscopic changes in the material with radiation and subsequent changes with time. The introduced models

[1] The term "diffusion" used here is more a descriptive one combining effects like diffusion, migration, break-up, re-configuration of defects or better reactions between defects propagating through lattice – also often summarized by the term "annealing".

F. Hartmann, *Evolution of Silicon Sensor Technology in Particle Physics*,
Springer Tracts in Modern Physics 275, DOI 10.1007/978-3-319-64436-3_2

describe the evolution of sensor parameters like leakage current, depletion voltage and **C**harge **C**ollection **E**fficiency CCE. A significant dependency on the type of radiation particle exists. In addition, for charged particles, a strong dependence is seen for different irradiated silicon materials – especially on their oxygen or carbon content. The models, with the initial constants, describe the data very well. But for a large production, it is strongly advised to launch a dedicated radiation campaign allowing subsequently the re-fit of Hamburg model parameters for the specific sensors.

2.1.1 Damage by Particles

Traversing particles are not only ionising the lattice but they also interact with the atomic bodies via the electromagnetic and strong forces. Atoms are displaced and create interstitials I, vacancies V and more complex constructs, e.g. di-vacancies V_2 or even triple-vacancies V_3, also di-interstitials I_2 are common. All these defects deform the lattice. Some examples are depicted in Fig. 2.1. In addition diffusing Si atoms (interstitials I) or vacancies often form combinations with impurity atoms, like oxygen, phosphorus or carbon, again with different properties. All these lattice displacements populate new levels in the band gap, changing the initial silicon properties.

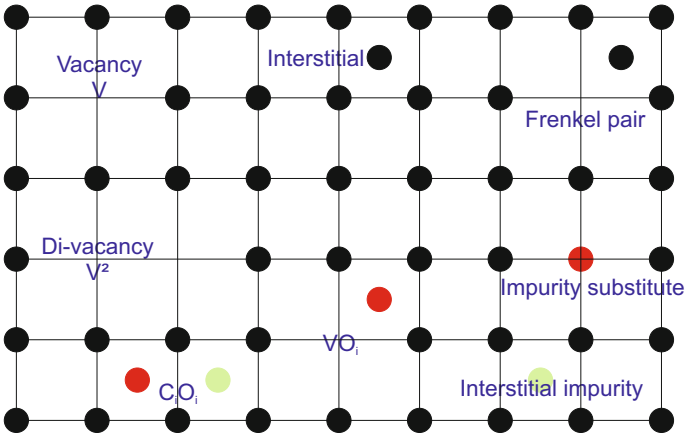

Fig. 2.1 The figure shows an exemplary selection of atomic displacements in the lattice after collision with traversing particles. These vacancies, interstitials and complex clusters are creating new levels in the energy scheme of the semiconductor and therefore change the elementary properties. As abbreviation, vacancies are labeled V, interstitials I, di-vacancies V_2. Impurities are labeled with their atomic sign, their index defines their position as substitute or interstitial, e.g. C_s or C_i

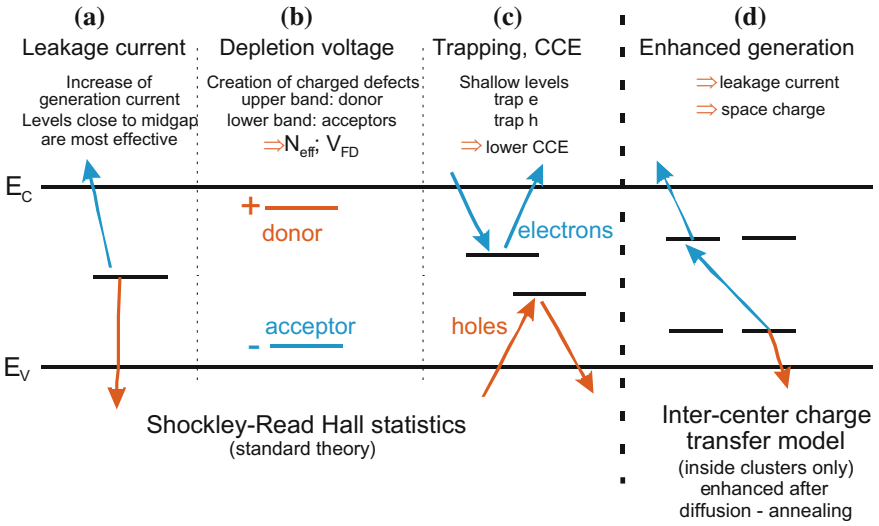

Fig. 2.2 The different defect level locations and their effects. All relevant defect levels due to radiation are located in the forbidden energy gap. **(a)** Mid-gap levels are mainly responsible for dark current generation, according to the Shockley–Read–Hall statistics and decreasing the charge carrier lifetime of the material. **(b)** Donors in the upper half of the band gap and acceptors in the lower half can contribute to the effective space charge. **(c)** Deep levels, with de-trapping times larger than the detector electronics peaking time, are detrimental. Charge is "lost", the signal decreases and the charge collection efficiency is degraded. Defects can trap electrons or holes. **(d)** The theory of inter-centre charge transfer model says that combinations of the different defects in so-called defect clusters additionally enhance the effects

The resulting macroscopic property changes are

- increase of dark current
- change of depletion voltage level (N_{eff}) due to creation of mainly additional acceptor levels
- decrease of charge collection efficiency due to defect creation, acting as traps

The basic important levels and their roles and macroscopic effects are shown in Fig. 2.2. Defect analysis and even defect engineering was started in the R&D collaboration Rose/RD48[2] and is nowadays continued within the RD50 collaboration at CERN. Within this chapter the basic mechanisms are described, special cases and defect engineering will be described in Sects. 6.4.2 and 7.1.1. The topic of defect engineering is fully covered and up to date in [336]. For example vacancy plus phosphorus *VP* removes the donor property of single phosphorus. A special case is the di-vacancy plus oxygen combination V_2O, which introduces additional negative space charge. A detailed table of defect combinations and respective quantitative energy levels can be found in [194, 219]. The defect distribution and clustering in

[2]ROSE: **R**&**D** **O**n **S**ilicon for future **E**xperiments.

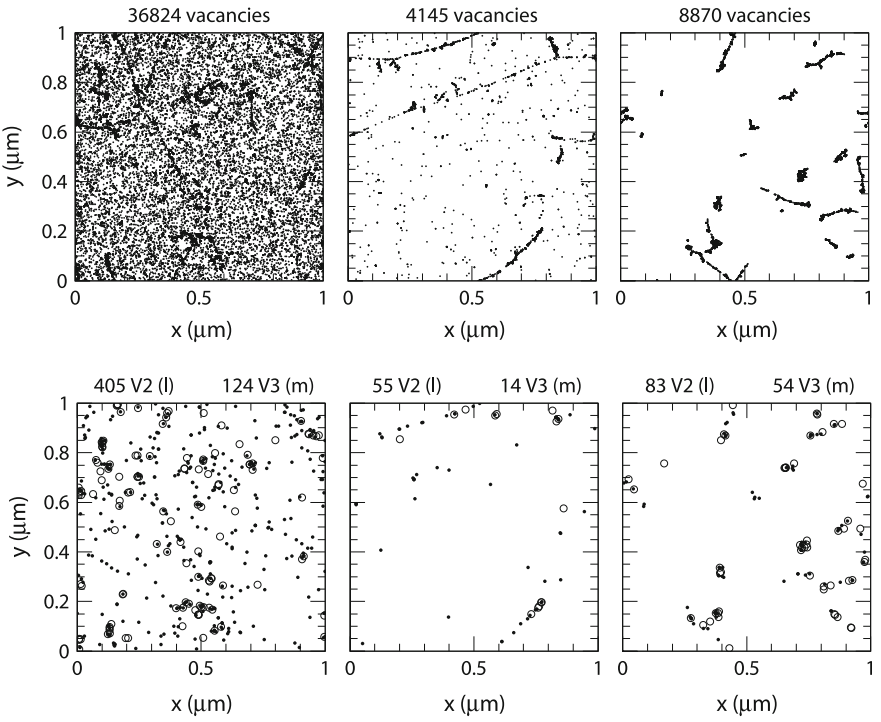

Fig. 2.3 Simulation of defect formation with radiation and diffusion. The upper three simulations show the microscopic picture of defect distribution. About 10 MeV protons (*left*) produce a quite homogeneous vacancy distribution, while more energetic protons with 24 GeV (*middle*) form more clustered and discrete defects. Neutrons with 1 MeV (*right*), interacting only due to strong interaction, do produce more isolated clustered defects. The plots are projections over 1 µm of depth (z) and correspond to a fluence of 10^{14} $n_{1\mathrm{MeV}}/\mathrm{cm}^2$. The *lower three* figures are displaying final constellations after a certain annealing time and therefore diffusion effects occurred. Many initial defects decay, e.g. Frenkel pairs, where interstitials recombine with vacancies. Others form more local clusters, like formations of di- and triple vacancies, with again different levels and therefore different properties. The full study is described in [150]

Fig. 2.3 clearly show the difference between irradiation with charged and neutral particles and different energy levels that emerge from them. Especially the additional Coulomb force of a charged particle enhances small energy transfer and therefore local short distance defects, known as Frenkel pairs. Neutral particles, like neutrons, acting via the strong force result mainly in long-range cluster defects. With enough energy the initial **P**rimary **K**nock on **A**tom PKA acts further on several additional lattice atoms. In the non-relativistic approach, the maximum transferred energy $E_{R,max}$ can be calculated in the case of recoil for a particle with mass m_p and kinetic energy E_p with

$$E_{R,max} = 4E_p \frac{m_p m_{Si}}{(m_p + m_{Si})^2} \tag{2.1}$$

For electrons with energy E_e and mass m_e, higher kinetic energies are needed for lattice damage. $E_{R,max}$ can be calculated by the approximate relativistic relation

$$E_{R,max} = 2E_e \frac{E_e + 2m_e c^2}{m_{Si} c^2} \tag{2.2}$$

Table 2.1 shows the average and maximum energy transfer of different particle types with the incident energy of 1 MeV.

Also, the energies needed to knock an atom from its original lattice place are clearly dependent on the binding forces and therefore on the material. In the case of silicon, the minimum energy needed to displace a single lattice atom (Frenkel pair) is $E_{\text{single defect}} \approx 25$ eV, while $E_{\text{cluster}} \approx 5$ keV [343] is needed to produce a defect cluster. Table 2.2 lists the minimum kinetic particle energies needed to transfer $E_{\text{single defect}}$ or E_{cluster}, subsequently creating a single point defect or a cluster.

The **N**on **I**onising **E**nergy **L**oss NIEL hypothesis allows a first-order normalization of radiation damage with respect to different particles with different energies, see also Table 2.2. According to NIEL, the damage manifestation depends only on energy transferred in collisions regardless of particle energy and type. We will see later that this is not always true.

The displacement damage $D(E)$ can be calculated by

$$D(E) = \sum_i \sigma_i(E_{kin}) \int_0^{E_{R,max}} f_i(E_{kin},\ E_R) P(E_R) dE_R \tag{2.3}$$

where all possible interactions are summed up. σ_i is the cross-section of the process and $f_i(E, T)$ is the probability of having a collision of a particle with E_{kin}, transferring a recoil energy of E_R. $P(E_R)$ is the Lindhard partition function [190], describing

Table 2.1 Maximum energy transfer ($E_{Recoil,max}$) versus average ($E_{Recoil,av}$) of different particle types with incident energy of 1 MeV. Clearly the long-ranging Coulomb force favours a small energy transfer and therefore point defects, while the strong force produces mostly clusters

	Electron	Proton	Neutron	Si^+
Force	Coulomb	Coulomb and nuclear	Elastic nuclear	Coulomb
$E_{R,max}$[keV]/$E_{R,av}$[keV]	0.155/0.046	133.7/0.21	133.9/50	1000/0.265

Table 2.2 The minimum kinetic particle energies to create single point or cluster defects can be derived with formula 1.45 (p and n) and 1.46 (e^-). The ^{60}Co-photons could only create a cluster defect via a secondary electron (dominantly via Compton effect), but it cannot energize e^- up to 8 MeV

Particle	$E_{\text{single defect}}$	E_{cluster}
neutron; protons	185 eV	35 keV
electrons	225 keV	8 MeV
^{60}Co-gammas	1 MeV	No cluster

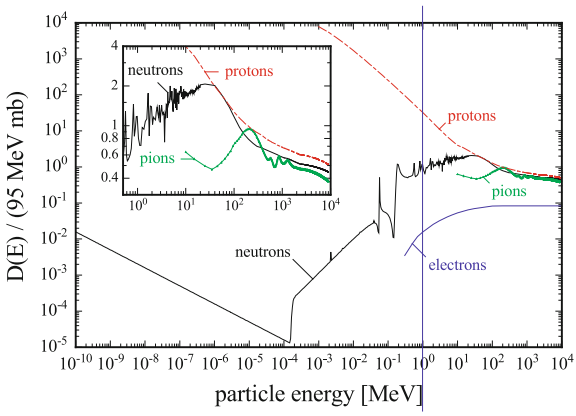

Fig. 2.4 NIEL – non ionising energy loss. Displacement damage function D(E) normalized to 95 MeVmb for neutrons, protons, pions and electrons. The inserted graph shows a detail of the figure around relevant energies for high energy physics [150, 219]

the fraction of energy going into silicon atom displacement, e.g. $P(E_R) \approx 50\%$ for 10 MeV protons or $P(E_R) \approx 42\%$ for 24 GeV protons and $P(E_R) \approx 43\%$ for 1 MeV neutrons [150]. The resulting displacement functions are plotted in Fig. 2.4. As standard the 1 MeV *neutron equivalent fluence* $[n_{1\mathrm{MeV}}/\mathrm{cm}^2]$ is used and abbreviated with Φ_{eq}, corresponding to $D_{neutron}$ $(1\,\mathrm{MeV})/\mathrm{cm}^2 = 95\,\mathrm{MeV\ mb/cm}^2$, with millibarn: $\mathrm{mb} = 10^{-27}\mathrm{cm}^2$. It is therefore possible to scale radiation damage from different particles and different energies by a simple numerical factor κ to make comparison possible. κ is defined as the ratio of the individual damage particle factor for a given energy and 1 MeV neutrons.

$$\kappa = \frac{\int D(E)\phi(E)dE}{95MeV\,mb \cdot \Phi} = \frac{\Phi_{eq}}{\Phi} \tag{2.4}$$

where $\phi = \int \phi(E)dE$ is the irradiation fluence. The 1 MeV neutron equivalent fluence Φ_{eq} is then calculated by

$$\Phi_{eq} = \kappa\Phi = \kappa \int \phi(E)dE; \quad [\Phi_{eq}] = n_{1\ \mathrm{MeV}}/\mathrm{cm}^2 \tag{2.5}$$

In plots and in literature the $n_{1\,\mathrm{MeV}}/\mathrm{cm}^2$ unit is often omitted and without specific reference to a particle type all fluences are given as 1 MeV neutron equivalent.

Leakage Currents

Mid-gap defects are constantly produced during radiation. They degrade mainly the lifetime τ, being efficient electron–hole pair generators they therefore increase the dark currents. It was found in many experiments that there is a linear behaviour of dark current versus fluence. The shot noise increases with $ENC_{IL}\sqrt{I}$ respectively; see also Sect. 1.5.

$$\frac{\Delta I}{V} = \alpha\Phi_{eq} \tag{2.6}$$

where V normalizes for a given volume. α is called the current-related damage rate. The correspondence is shown in the left part of Fig. 2.5. The good linearity over several orders of magnitude allows the technical use of diodes to determine the particle fluence by the increase of current.

Depletion Voltage

The situation for the effective space charge concentration is a bit more difficult. It is displayed in Fig. 2.6. Starting with an n-type-doped silicon bulk, a constant removal of donors ($P + V \rightarrow VP$ centre) together with an increase of acceptor-like levels (one example is $V + V + O \rightarrow V_2O$) shifts the space charge first down to an intrinsic level and then up to a more p-like substance. The material "type inverts". When the material changes from n to p, the space charge changes sign this is often referred to as **S**pace **C**harge **S**ign **I**nversion – SCSI. The depletion voltage therefore drops first and starts rising later. Figure 6.28 in Sect. 6.4.2 shows an example of the CMS sensor irradiation campaign and the evolution of depletion voltage.

$$N_{eff} = N_{D,0}e^{-c_D\Phi_{eq}} - N_{A,0}e^{-c_A\Phi_{eq}} - b\Phi_{eq} \tag{2.7}$$

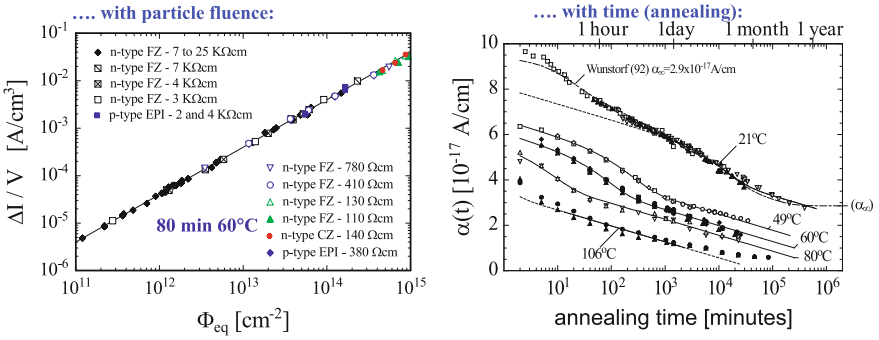

Fig. 2.5 Leakage current versus fluence and annealing time [219, 356]

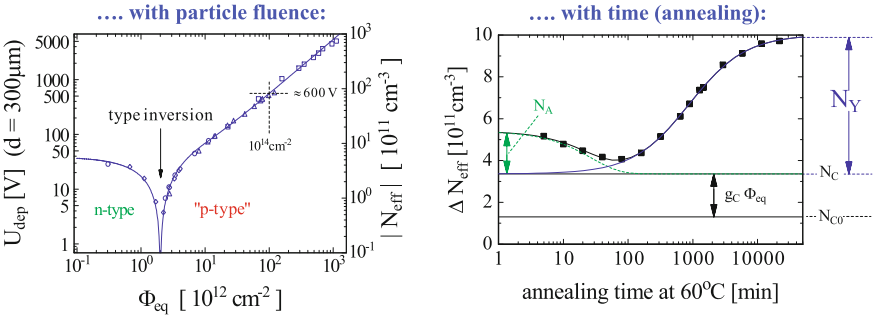

Fig. 2.6 Depletion voltage versus fluence and annealing time [219]

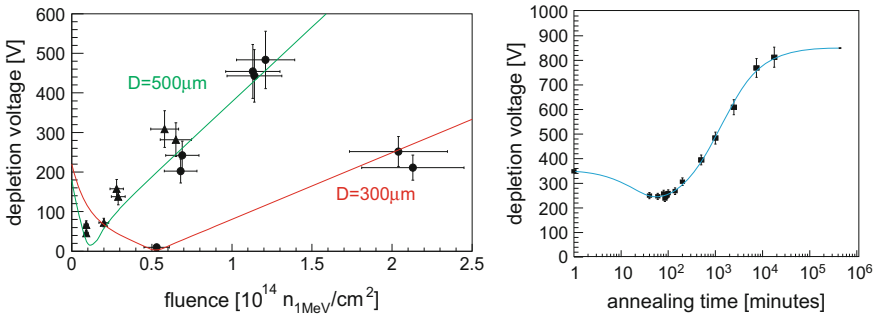

Fig. 2.7 Evolution of V_{FD} for different fluences and annealing durations. To have a basis for radiation evaluation, CMS irradiated several sensors and modules to get actual adapted fit parameters to the Hamburg model for the specific procured sensors. In this case, the beneficial constants g_a were found to be $(1.11 \pm 0.16) \cdot 10^{-2}\ \mathrm{cm}^{-1}$ and $t_a(60°\mathrm{C}) = 21 \pm 8$ min; the reverse constants are $\mathrm{g}_Y = 4.91 \pm 0.27 \cdot 10^{-2}\ \mathrm{cm}^{-1}$ and $\mathrm{t_y}(60°\mathrm{C}) = 1290 \pm 262$ min. The different $\mathrm{V_{FD}}$ curve behaviours in the *left plot* can be explained by the different sensor thicknesses of D =500 µm (*upper curve*) and 320 µm (*lower curve*) – mind $\mathrm{V_{FD}} \sim \mathrm{N_{eff}} \cdot \mathrm{D}^2$. At fluences of $\Phi_{eq} = 10^{14}\ n_{1\mathrm{MeV}}/\mathrm{cm}^2$, $\mathrm{V_{FD}}$ of the thick sensor would have increased above 1000 V. The initial compatible $\mathrm{V_{FD}}$ values are due to the different sensor resistivities. Data are compared to calculations for an annealing time of 80 min and an annealing temperature of 60 °C at each fluence step. More about this study is described in Sect. 6.4.2 and [351]

With the evolution of N_{eff} can be parameterized in first approximation with the donor and acceptor removal rates c_D and c_A plus the most important acceptor creation term $b\Phi_{eq}$. Since there is a significant temperature-dependent diffusion, Formula (2.13) parameterizes the evolution in a more common and general description.

Charge Trapping

The trapping rate is proportional to the concentration of trapping centres N_i, resulting from defects. Therefore the trapping probability can be formulated by

$$\frac{1}{\tau_{eff}} = \sum_i N_i (1 - P_i) \sigma_i v_{th} \tag{2.8}$$

with P_i the occupation probability and σ_i the charge carrier cross-section. In first order the fluence dependence is linear and can be written as

$$N_i = g_i \Phi_{eq} f_i(t) \Rightarrow \frac{1}{\tau_{eff}} = \gamma \Phi_{eq} \tag{2.9}$$

with the introduction rate g_i; $f_i(t)$ describes the annealing with time. An example is plotted in Fig. 2.9 (left side). The slope is different for electron and hole trapping, they are differently affected due to their different mobilities. Some initial numbers for proton and neutron irradiations are given in Table 2.3. The degradation of **C**harge **C**ollection **E**fficiency CCE can then be described by

Table 2.3 Introduction of trapping centres, significant for electrons and holes of neutron and proton radiations [184]

	$\gamma_{e,0}$ [10^{-16} cm^2/ns] for Electron	$\gamma_{h,0}$ [10^{-16} cm^2/ns] for Holes
Fast charged hadrons	(4.97 ± 0.14)	(5.25 ± 0.17)
Neutron	(3.53 ± 0.24)	(5.10 ± 0.39)

$$Q_{e,h}(t) = Q_{0_{e,h}} e^{-\frac{t}{\tau_{eff_{e,h}}}}, \text{ where } \frac{1}{\tau_{eff_{e,h}}} \propto N_{\text{defects}} \tag{2.10}$$

The above assumption is valid as long as the drift velocity v_D is much smaller than thermal velocity vth and trapping distance $\lambda = v_{th} \cdot tau_{eff}$. At effective fluences of $\Phi_{eq} = 10^{15}\ n_{1\text{ MeV}}/\text{cm}^2$ and above, trapping becomes the most limiting factor of silicon usage as a particle detector. The charges no longer arrive at the collecting electrodes in 300 µm thick sensors. Examples of charge travelling distances x for $\Phi_{eq} = 10^{15}\ n_{1\text{MeV}}/\text{cm}^2$ and $\Phi_{eq} = 10^{16}\ n_{1\text{MeV}}/\text{cm}^2$ are

- $\tau_{eff}(10^{15}\ n_{1\,\text{MeV}}/\text{cm}^2) = 2\,\text{ns} : x = v_D \cdot \tau_{eff} = (10^7\text{cm/s}) \cdot 2\,\text{ns} = 200\,\mu\text{m}$
- $\tau_{eff}(10^{16}\ n_{1\,\text{MeV}}/\text{cm}^2) = 0.2\,\text{ns} : x = (10^7\text{cm/s}) \cdot 0.2\,\text{ns} = 20\,\mu\text{m}$

The following list summarizes the main operation limiting effects of radiation bulk damages for the different Φ_{eq} levels:

- at $10^{14}\ n_{1\,\text{MeV}}/\text{cm}^2$ the main problem is the increase of leakage current
- at $10^{15}\ n_{1\,\text{MeV}}/\text{cm}^2$ the high resulting depletion voltage is problematic
- at $10^{16}\ n_{1\,\text{MeV}}/\text{cm}^2$ the fundamental problem is the CCE degradation.

2.1.2 Annealing – Diffusion of Defects

Interstitials and vacancies are very mobile at temperatures $T > 150\,\text{K}$. The lower part of Fig. 2.3 displays the result of defect diffusion. Basically, there is the possibility of

- Frenkel pair recombination ($I + V \rightarrow Si$)
- multi-vacancy and multi-interstitial combination (e.g. $V + V \rightarrow V_2$)
- combination of more complex defects (e.g. $C_i + O_i \rightarrow C_i O_i$ or $V + P \rightarrow VP$)

where the former types are short-range and very mobile processes and therefore happen with a shorter time constant, while the latter happens with a longer time constant. The whole process is called *annealing* with a beneficial part reducing the damage and a reverse annealing part degrading macroscopic sensor properties. Some parts are stable and do not evolve with time. The diffusion processes are naturally temperature dependent and some effects, e.g. depletion voltage evolution, can even be effectively frozen out at temperatures below 0 °C. In addition, different levels in the energy band behave differently with respect to time constants and temperatures.

Table 2.4 α and τ_I for different temperatures

Annealing temperature in °C	21	40	60	80
α_0 in 10^{-17} A/cm	7	6	5	4
τ_I in min	140000	260	94	9

The table shows the α parameter and the time constants τ_I for the current annealing for different temperatures. Below room temperature the time constants are longer than 100 days and annealing is almost frozen out

Annealing – Leakage Current

The annealing of the dark currents is displayed in the right part of Fig. 2.5.

The α parameter, respectively the dark currents, can be parameterized. In first order α can be fitted by a sum of exponentials, pointing to the existence of several contributing defects with different decay time constants. The radiation afflicted current continuously decays exponentially until it follows more or less a logarithmic behaviour or even saturates for higher temperatures after several months. According to [219] the annealing behaviour can be described by

$$\alpha = \alpha_0 + \alpha_I e^{-\frac{t}{\tau_I}} - \beta \cdot ln\frac{t}{t_0} \tag{2.11}$$

with $\alpha_I \sim 1.25 \cdot 10^{-17}$ A/cm, $\beta \sim 3 \cdot 10^{-18}$ A/cm and $t_0 = 1$ min. τ_I takes the annealing temperature T_α dependence into account, where

$$\frac{1}{\tau_I} = k_{0I} \cdot e^{\frac{E_g}{k_B T_\alpha}} \tag{2.12}$$

with $k_{0I} = 1.2^{+5.3}_{-1.0} \cdot 10^{13}$ s^{-1}, e.g. $\tau_I \approx 10$ days at room temperature. $\alpha_0 = -(8.9 \pm 1.3) \cdot 10^{-17}$ A/cm $+ (4.6 \pm 0.4) \cdot 10^{-14}$ AK/cm $\cdot \frac{1}{T_\alpha}$ is a fitted parameter dependent on the annealing temperature. Table 2.4 gives α and T_I examples for different temperatures.

The average α after a standard annealing scenario of 80 min at 60°C is $4 \cdot 10^{-17}$ A/cm, measured at T = 20°C. The α value changes about 15% every 1 degree. The effect is temperature dependent and also effective but strongly reduced at sub-zero temperatures. Different from the time dependence of the depletion voltage, which starts to rise at later times, the current annealing always decreases the dark current and is therefore only "beneficial".

Annealing – Depletion Voltage

The annealing of N_{eff} and therefore the depletion voltage evolution can be described by

$$\Delta N_{eff}(\Phi_{eq}, t, T) = N_{C,0}(\Phi_{eq}) + N_A(\Phi_{eq}, t, T) + N_Y(\Phi_{eq}, t, T) \tag{2.13}$$

where Φ_{eq} stands for 1 MeV neutron equivalent fluence, with the stable term $N_{C,0}$, the short-term annealing term N_A and the second-order long term N_Y. This description is called the Hamburg model and it is depicted in the right part of Fig. 2.6. In its basic nature it parameterizes the space charge change due to donor removal plus acceptor creation with fluence and latter annealing. It was proposed in [219] and with some adaptation of the initial time constants to the different sensors it has been very successful.

Before discussing the three annealing terms in some detail, it must be mentioned that the stable term is the most relevant one in a high-radiation environment. For the LHC experiments, the beneficial annealing needs to be exploited during the maintenance periods to heal the short-range defects and therefore reduce the depletion voltage, while the reverse annealing term needs to be suppressed by freezing out at sub-zero temperatures, both are possible. It also has to be mentioned that all constants in this chapter are taken from [219] and need to be re-fitted for the user case, see e.g. [350], some constants reflect, for example, the oxygen content. As an example, Fig. 2.7 illustrates the CMS radiation campaign, where sensors were subjected to several fluences and annealing parameters were fitted.

The Stable Term $N_{C,0}$

In the current understanding, the stable damage term consists of two components, the donor removal and the acceptor creation rate.

$$N_C(\Phi_{eq}) = N_{C,O}(1 - e^{-c\Phi_{eq}}) + g_c\Phi_{eq} \tag{2.14}$$

where c is the initial dopant (donor in n- and acceptor in p-bulk) removal constant and $N_{C,O}/N_{eff,non\text{-}irradiated}$ is the fraction of initial dopant removal, depending strongly on the oxygen concentration, where oxygen can bind vacancies, which would otherwise combine with phosphorus ($V + O \rightarrow VO$ instead of $V + P \rightarrow VP$). This is of course grandly simplified.

Michael Moll – spokesperson of the RD50 collaboration responds to this subject:

> For p-in-n sensors, the donor removal component of the Hamburg model can not be described by a simple process $V + P \rightarrow VP$ only. There is something more behind that and we still do not exactly understand what it is.

Ranges from 10 to 80% donor removal are observed after neutron irradiation in p-in-n sensor. On average the initial donor removal rate here is $N_{C,0} \cdot c = (7.5 \pm 0.6) \cdot 10^{-2}\ \mathrm{cm}^{-1}$. The second term describes a creation rate of stable acceptors with an average measured $g_c = (1.49 \pm 0.04) \cdot 10^{-2}\ \mathrm{cm}^{-1}$. Neither terms are time dependent as there are no evolutionary diffusion processes.

The Short-Term Annealing N_A, the Beneficial One

Monitoring the sensors directly after irradiation, a fast change of the depletion voltage can be observed. For type-inverted material V_{FD} decreases with time, while it increases before type inversion. This can easily be interpreted as an increase of the effective doping concentration N_{eff}. The introduced acceptors decay and inverted

sensors with negative space charges become less negative while sensors that are not type inverted with positive space charge become more positive.[3] The decay of defects can be factorized in a series of first-order exponential decays. In extremely long duration HEP experiments, the short time constants of minutes and hours are not relevant and the series can be reduced to

$$N_A(\Phi_{eq}, t) = \Phi_{eq} g_a e^{-\frac{t}{\tau_a}}; \quad N_A = g_a \Phi_{eq} \tag{2.15}$$

The average value of $g_a = (1.81 \pm 0.14) \cdot 10^{-2}$ cm^{-1} was determined. The time constants τ_a, describing diffusion processes, are naturally temperature dependent and can be parameterized by

$$\frac{1}{\tau_a} = k_a = k_{0a} \cdot e^{-\frac{E_{aa}}{k_B T_a}} \text{ with } E_{aa} = (1.09 \pm 0.03) \text{ eV and } k_{0a} = 2.4^{+1.2}_{-0.8} \cdot 10^{13} \text{ s}^{-1} \tag{2.16}$$

They are summarized in Table 2.5 together with the time constants τ_y describing the reverse annealing term.

The Long-Term Annealing N_Y, the Reverse One

After a long time another first-order effect,[4] with another time constant τ_y, becomes effective – reverse annealing. Space charge becomes even more negative, more acceptor levels form. Reverse annealing can be parameterized by

$$N_Y = N_{Y,0} \cdot (1 - e^{-t/\tau_Y}) \tag{2.17}$$

with

$$N_{Y,0} = g_Y \cdot \Phi_{eq} \tag{2.18}$$

being directly proportional to the particle fluence, with the introduction rate g_Y depending on the radiation type and radiated sensor material, e.g. neutron radiation on standard n-type FZ has $g_{Y,neutron} = 4.8 \cdot 10^{-2}$ cm^{-1}. Time constants are given in Table 2.5. The diffusion is temperature dependent and can be described after [219] by

$$\frac{1}{\tau_Y} = k_Y = k_{0,Y} \cdot e^{-\frac{E_{YY}}{k_b T_a}} \text{ with } k_{0,Y} = 7.4 \cdot 10^{14} \text{ s}^{-1} \text{ and } E_{YY} = 1.31 \text{ eV} \tag{2.19}$$

[3] Reminder: acceptors are introducing negative, donors respectively positive, space charge.

[4] Reverse annealing is also often described in literature (e.g. [107, 266, 267]) as a second-order effect with a parameterization of $\left[1 - \frac{1}{1+t/\tau_y}\right]$, describing accurately N_{eff} versus time for long annealing times at higher temperatures. Nevertheless, the physical mechanism is ruled out due to the missing dependency of the effect on fluence. The rate, depending on the probability of **two** defects combining, does not increase with the number of defects.

Table 2.5 Annealing time constants; beneficial and reverse annealing [219]

Annealing temperature (°C)	−10	0	10	20	40	60	80
Short-term annealing τ_a	306 d	53 d	10 d	55 h	4 h	19 min	2 min
Reverse annealing τ_Y	516 y	61 y	8 y	475 d	17 d	21 h	92 min

The numbers define immediately the running and maintenance conditions of experiments in a high-radiation environment. Operation temperatures below 0 °C freeze out the reverse term completely and largely the beneficial one. During the maintenance periods the detectors temperatures should be elevated in a controlled way to benefit from the short-term annealing and to absolutely avoid the reverse one. An example of the foreseen maintenance scenarios of CMS are described in Sect. 6.4.2

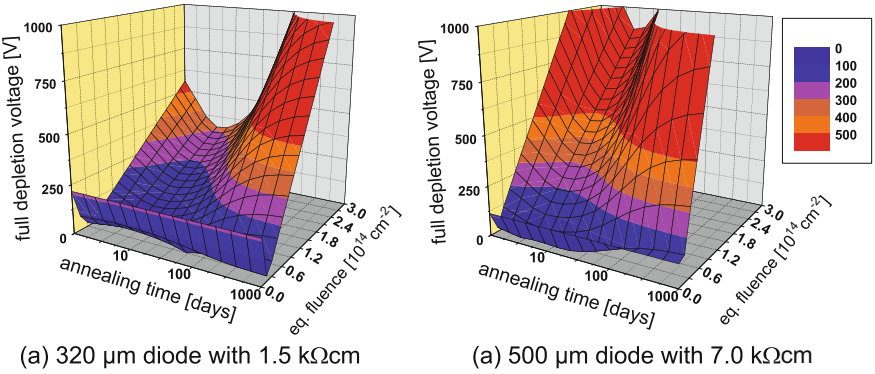

Fig. 2.8 Depletion voltage versus fluence and annealing time at room temperature. The plot shows the simulated depletion voltages according to the Hamburg model for 300 and 500 µm thick silicon, the two CMS sensor configurations. The ordinate shows the depletion voltage versus fluence and temperature. For detector operation in high-radiation environment, it is clearly necessary to make use of the annealing up to the point where the reverse annealing becomes too strong. Of course there is one plot to be drawn per temperature, which defines the annealing time constants [80]

The full depletion voltage evolution with respect to fluence and time for a fixed temperature is presented in a condensed form in Fig. 2.8.

Annealing of Effective Trapping Probability

Formula (2.9) [175] already introduced the term $f_i(t)$ and the proportional factor γ. Experimental data show a decreasing probability of electron trapping and an increase of hole trapping in time. The right part of Fig. 2.9 shows the annealing of the effective inverse trapping times. The interesting operational parameter **C**harge **C**ollection **E**fficiency CCE is then basically proportional to the electric field and trapping.

$$\gamma(t) = \frac{1}{\tau_{eff}} = \frac{1}{\tau_0} \cdot e^{-\frac{t}{\tau_a}} + \frac{t}{\tau_\infty}(1 - e^{\frac{t}{\tau_a}}) \tag{2.20}$$

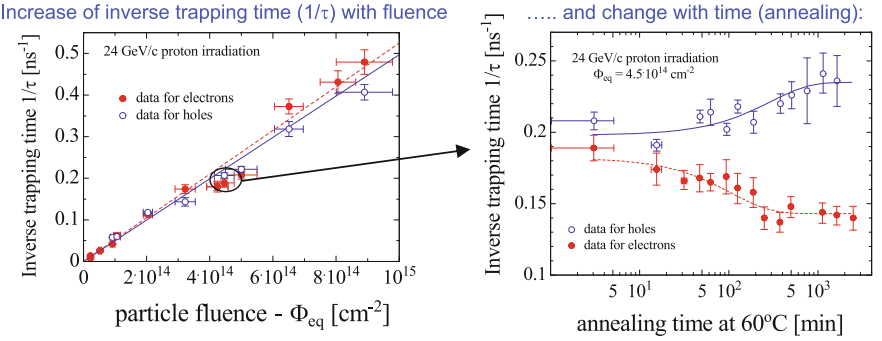

Fig. 2.9 Trapping time versus fluence and annealing time [184]

Still today, the statistical sample is not large, especially not on low-temperature samples. Saturation already starts after several hours at $T = 60\,^{\circ}\mathrm{C}$, when the annealing time constants τ_a for electrons and holes are on the order of hours at elevated temperatures. The effect counts for roughly 20% for electrons and 20 – 50% for holes. It can be neglected at sub-zero temperatures. Pixel detectors[5] at ATLAS and CMS even benefit from the fact that inverse trapping times decrease for electrons and therefore CCE increases with time.

To summarize, the macroscopic changes deriving from diffusion, called annealing, are highly temperature dependent, while frozen out at sub-zero temperatures they are dominant at room temperature and above. Leakage current, **C**harge **C**ollection **E**fficiency CCE and depletion voltages evolve with time in the following way:

- leakage current always decreases
- trapping probability decreases for holes and increases for electrons
- acceptor levels first decay in the beneficial phase and increase later in the reverse annealing phase. This leads to an increase/decrease of depletion voltage before and decrease/increase after type inversion.

The recipe is to benefit from the beneficial annealing for voltage and current and avoid the reverse annealing phase to stay in applicable bias voltage levels.

2.2 Defect Analysis, New Materials and Detector Engineering

It was mentioned, in the last sections, that impurities can influence the radiation hardness. Due to meticulous studies, mostly in the framework of RD48 [191] and RD50 [336], several influences are understood at the microscopic level or at least

[5] ATLAS and CMS pixels use n-in-n technology where most of the charge is induced by electrons, while for standard strip p-in-n sensors most of the charge is induced by holes.

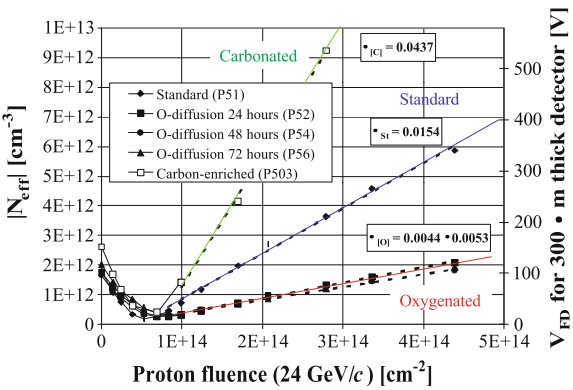

Fig. 2.10 Evolution of V_{FD} versus time of differently engineered silicon diodes. The beneficial influence of oxygen and malevolent effect of carbon are clearly visible. Today the ATLAS and CMS pixel sensors are composed of oxygenated silicon sensors [Courtesy of RD48 [191] and RD50]

empirically on the macroscopic level. A lot of different silicon sensor substrates with several types of diffused atoms were investigated, e.g. oxygenated, carbonated, *Li*-covered, etc. Substrates created with different growth techniques were investigated and irradiated to several fluence levels, e.g. FZ, CZ, magnetic[6] CZ, epitaxial material. To present all studies is beyond the scope of this book but a fair number of examples from RD50 will be described in the next paragraphs. The discussion of final sensor choices for the CMS Tracker Upgrade for the HL-LHC will be presented in Sect. 7.1 in detail.

Today, the most important beneficial effect identified was, that for oxygen-enriched material, the stable damage parameter g_c decreased and the reverse annealing time constant τ_Y increased. However, this effect is only valid for irradiation by charged particles.[7] The effect is already being technologically exploited. Today, the pixel sensors of the ATLAS and CMS experiment are oxygenated. The beneficial effect of high oxygen concentration and the degrading effect of carbon content are shown in Fig. 2.10.

The next paragraphs *introduce* the study of microscopic effects and their impact on macroscopic parameters and the fact that NIEL is no longer valid for N_{eff}, nor for effective trapping times, for different materials; depletion voltage becomes an academic concept, how sensors behave at very high fluences, and briefly discuss the effect of amplification in HEP sensor prototypes. In general, investigations are ongoing and the understanding of radiation damage mechanism and device engineering is growing every day.

[6] mCz: CZ crystal growth in a magnetic field to achieve a homogeneous oxygen distribution.

[7] Note that this violates the NIEL hypothesis.

2.2.1 Study of Microscopic Defects and Their Impact on Macroscopic Parameters

Meticulous studies about defects induced by radiation have been conducted in the RD50 and WODEAN [354] framework. The goal is to answer the following questions for microscopic defects:

- correlation between chemical constellation and energy level; e.g. VO-complex at $E_C - 0.176eV$, or E5 seems to be a tri-vacancy-complex [160]. Not much is known for more complex structures
- correlation between defects and macroscopic effects (operations/measurement) – (a) Leakage current? (b) Space charge (Donor? Acceptor? Neutral?)?, (c) Trapping?
- which are point or cluster defects?
- how do they evolve with time (annealing)? Differently said, which defects are responsible for reverse annealing?
- are they charged or neutral at operation temperature?
- which particles (p, π, n, γs and e radiation) at which energy induce which defects? NIEL?
- Defect Engineering: which materials (FZ, DOFZ, Cz, mCz, Epi) are affected by which radiation type and which defects develop?
  - What can we do to avoid certain malicious defects? E.g. add oxygen since the VO complex has no negative effect and is stable.

A combination of radiation and measurement, standard mainly DLTS and TSC (both briefly introduced in Sect. 1.8), is shedding light on the topic. The phase space has not yet been exhaustively explored but more and more pieces of the puzzle have been identified in the past 2 decades. Figure 2.11 tries to summarise the different energy levels of certain defects and their role as we understand them.

A comprehensive set of corresponding publications can be found at [153]. Reference [250] tabulates the defects with their energies, cross-sections and the most recent understanding of their effects. Selected, relevant examples will be presented in the following paragraphs. Some examples of defects and their potential effects:

The I_P(0/-) point-defect is being generated with γ radiation and contributes to the leakage current. H116K(0/-), H140K(0/-), H152K(0/-) are the main culprits for the reverse annealing of the depletion voltage (more later). The current indications mark E205a(-/0) and H152K(0/-) as important trapping centres. It seems that oxygen binds vacancies and also the bi-stable BD is oxygen dependent with a higher introduction rate with proton than neutron irradiation. The E4/E5 are believed to triple-vacancy-complexes.

Two prominent and pedagogic examples of the microscopic to macroscopic correlations will be presented for illustration; a tiny fraction of the many studies. The understanding is continuously growing.

One example is presented, where levels H116K, H140K, H152K, as acceptors, can be identified being responsible for reverse annealing. These levels do not form

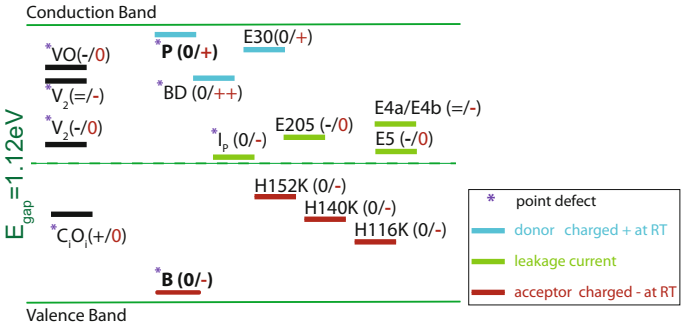

Fig. 2.11 A selection of radiation induced defects and their energy level in the band gap. To put everything in perspective, the levels of the common dopant atoms, phosphorus and boron, are given. The asterisk (*) indicates point defects, the others are more complex! The *upper right* indices gives the potential charge-states of the defects. The right value defines the space charge state of the defect in the SCR at room or operation temperature. Two examples: The free electron from the P atom (0/**+**) acts as majority charge carrier and the P is positively charged (*n*-doped). The VO-complex (-/**0**) is neutral – 0. "ZERO" means they are neutral; not active as dopants. Therefore the "*red*" defects (0/**-**) in the lower half act as acceptors and the upper "*blue*" defects (0/**+**) as donors. The left index value represents the defect state when a charge carrier has been trapped. Mind, for acceptors the free charge (carrier) occupying the trap is a hole and for donors it is an electron. The "*green*" defects, located near mid-band, contribute to the leakage current. The charge state transition from left to right is what we measure with DLTS (space charge change – capacitive change) or TSC (released charge – current). For example, the H152K(0/-) complex releases an electron measured as a current by TSC and space charge changes from neutral to positive, where DLTS measures the corresponding capacitive change

with γ radiation and are therefore cluster defects. The concentration of these levels increases with long-time annealing and are quantitatively compatible with negative space charge build-up (N_{eff} change). Figure 2.12(left) shows the Thermally Stimulated Currents Method TSC to determine the defect level concentrations while Fig. 2.12(right) shows the corresponding N_{eff} change. The goal of material defect engineering is now to either avoid the creation of these defects or to create counteracting donor effects with similar annealing behaviour.

E4a and E4b, bi-stable defects, have been discovered by [105]. A study, described in detail at [159], uses the bi-stability of the E4 effects to prove the strong correlation with the leakage current. This is visualised in Fig. 2.13.

Several diodes of different materials have been irradiated to moderate levels (regime where DLTS still works). Due to the bi-stability of the defect, the E4 concentration can be changed with charge injection. The DLTS spectra were recorded after three different steps: at first after annealing at 200 °C for 30 min, where both E4 levels annealed out completely (open squares), secondly after injection of 1 A/cm^2 forward current (full circles) which leads to a full recovery of both levels and finally after a subsequent annealing at 80 °C for 60 min (solid line), restoring the initial state of the spectrum. The leakage current clearly follows the E4 concentration. The very similar behaviour of E4a with respect to E4b suggests that both defect states are

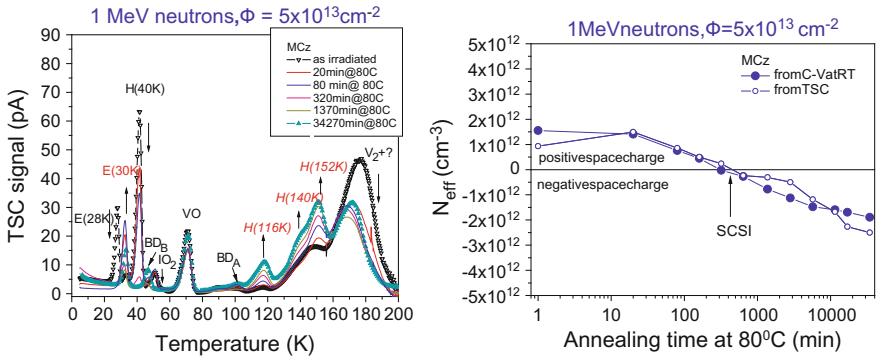

Fig. 2.12 Thermally Stimulated Currents Method scans were done after each annealing step. The rise of the microscopic levels H116K, H140K, H152K can be observed after each annealing step in the *left* figure while the *right* figure shows the corresponding change in depletion voltage (N_{eff}) for each annealing step, determined by the CV characteristic and a TSC scan [241]

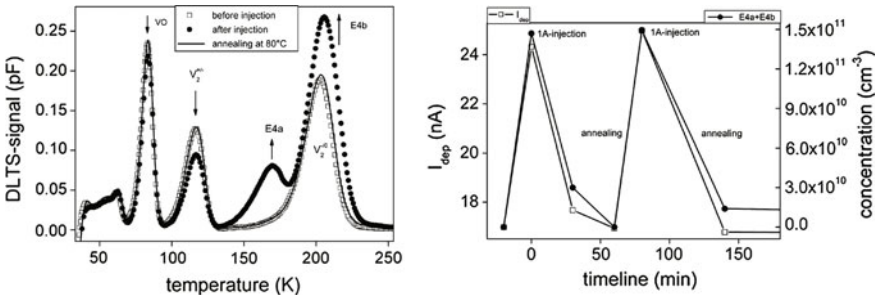

Fig. 2.13 The DLTS measurement on the *left* show a clear rise of the E4 concentration after current injection (1 A forward current) and a decrease to the original level after isothermal annealing of 80 °C. The leakage current strongly follows the E4 concentration, shown in the plot on the *right* [159]

the same defect complexes in a different "charge" state. Their annealing behaviour is similar to that of double-vacancies, suggesting that the complex is an n-vacancy complex.

The knowledge, which defects corresponds to which macroscopic parameter and which irradiation type introduces them, has grown considerably in the past decade. In addition the knowledge which defect is a point defect and which a cluster improves our understanding of the annealing process. All this can be fed, in a more simplistic way, into dedicated simulation and we start to achieve predicting power of parameter evolution with radiation and annealing.

2.2.2 *Different Materials and Different Radiation Types – NIEL Violation*

Already RD48 [191] proved the beneficial effect of high oxygen concentration in silicon material (DOFZ) with respect to depletion voltage evolution, violating the NIEL hypothesis – see also Fig. 2.10. This led to the exploitation of Czochralski material (Cz) and later to magnetic Czochralski (mCz[8]) where oxygen enrichment comes naturally during the melt process.

Radiation damage studies produced surprising results and in Fig. 2.14 no distinct SCSI point is present for these materials. After a long campaign of CV and TCT[9] studies, it became clear that with the new materials and with high fluences applied, one can no longer assume a linear electric field with one single junction at one side. A double peak or double junction can be qualitatively explained by two opposite linear fields at both ends defined by different space charge regions at both ends and possibly a zero or constant field region in the middle. More quantitatively, fits suggest a parabolic field throughout the sensor volume (more in the next Sect. 2.2.3). Often, with charge trapping, charges (TCT signals) drifting from the injection side are trapped before they reach the other side and double peaks are smeared out; thus a trapping corrected TCT analysis is mandatory.

As a result, the depletion voltage parameter becomes a more abstract concept and for high radiation levels, CCE or better signal-to-noise becomes the more realistic and important parameter[10] to measure. Consequently these are the main parameters evaluated for the HL-LHC upgrade program; see Sect. 7.1.1.

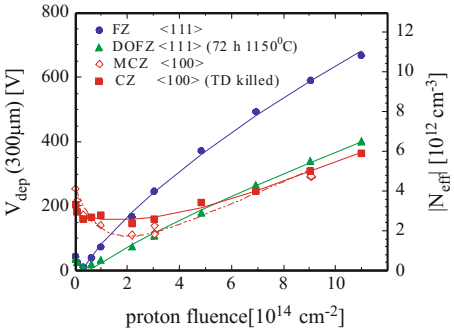

Fig. 2.14 Cz and mCz (*red points*) do not exhibit the distinct point of space charge sign inversion SCSI [220]

[8] An applied magnetic field during the melt creates an electric current distribution and an induced magnetic field. The active Lorentz force then dampens the oscillations in the melt, resulting in a more homogeneous oxygen distribution.

[9] In a **T**ransient **C**urrent **T**echnique TCT measurement the current slope represents the field and a sign change in slope indicates SCSI. Today we see a double peak thus a double junction (see also Fig. 1.48 and Sect. 2.2.3).

[10] With higher and higher "depletion voltages" even above a possible operation voltage, the only important parameter is the collected charge at the amplifier.

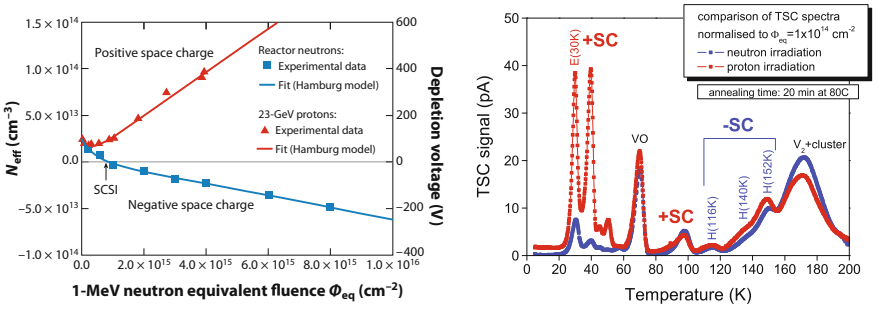

Fig. 2.15 Change of N_{eff} in EPI-DO material versus irradiation with different particles. Acceptor introduction is enhanced for neutron irradiation, similar to n-FZ material, while protons generate mainly donors [242]. In the corresponding study, with the Thermal Stimulated Current TSC method, the deep level states E30K have been identified to act as donors [158]

Furthermore, it has been realized that for some materials charged particles introduce distinctly different defects than neutrons. Figure 2.15 shows for EPI-DO (DO – diffused oxygen) the introduction of negative space charge after neutron irradiation with the corresponding SCSI. Instead, for protons, donor generation is enhanced (positive space charge) and therefore no SCSI is observed.

In the case of n-FZ sensors, both neutron and proton radiations introduce predominantly p-type defects. In the case of n-mCz, the neutrons introduce mainly acceptor (p-type) defects while charged particles produce mainly donors (n-type) defects – a clear violation of the NIEL hypothesis. This particular feature of the n-mCz silicon can have a favourable consequence on the degradation rate of the electrical properties of the detectors when the damage is due to a comparable mix of neutron and charged hadrons because the radiation induced defects can partially compensate each other [177]. To test this effect, n-in-n FZ and n-in-n mCz detectors have been irradiated with neutrons only, 25 MeV protons only and with an equal mix of neutrons and 26 MeV protons to a total dose of $1 \cdot 10^{15}$ $n_{1\text{MeV}}/\text{cm}^2$. Figure 2.16 shows the CCE(V) measurements of these devices and confirms the compensation effect. The two n-FZ detectors exhibit almost identical CCE(V) characteristics after the neutron, proton and mixed irradiations, while the n-mCz shows a faster rise of the CCE(V) in the case of mixed irradiation relative to the neutron and proton irradiations. The compensation effect of n-mCz is very interesting for locations/radii with similar radiation levels from neutrons and charged particles but, in reality, the location with the highest levels (inner radii) are largely dominated by charged particle radiation.

Another interesting plot showing the difference in annealing of FZ and mCz can be found in Fig. 7.17 on page 313.

The Role of Oxygen as we understand it

In the inner pixel detector, ATLAS and CMS are using sensors processed out of **D**iffusion **O**xygenated **F**loat-**Z**one DOFZ wafers. Materials with high oxygen concentration are high on the ingredients list for the future upgrades, due to the findings of RD48 & RD50. As shown in the previous and later sections higher oxygen

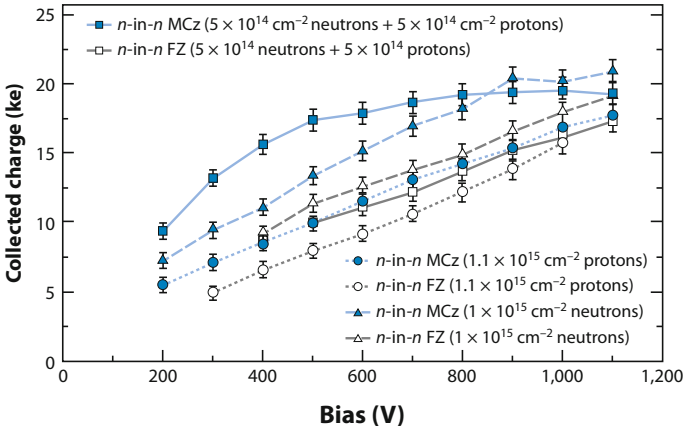

Fig. 2.16 Charge Collection Efficiency of mCz and FZ detectors after a total dose of $1 \cdot 10^{15}$ $n_{1\mathrm{MeV}}/\mathrm{cm}^2$ obtained with neutrons only, 26 MeV protons only or mixed (equal dose of neutrons and 26 MeV protons) irradiation. For FZ sensors (open bullets) neutron, proton or mixed irradiation give similar results at the same equivalent NIEL fluence – the mixed irradiation is just the average of protons and neutrons. For mCz (solid bullets), the picture is quite different – the mixed radiation shows a much higher CCE than either proton or neutron only, specifically at lower voltages. This is a clear indication of donor – acceptor *compensation* with the different radiation types (decrease of $|N_{eff}|$). At higher voltages, above depletion, the CCE difference becomes marginal

concentration seems to improve the radiation tolerance with respect to the change in depletion voltage (see e.g. Fig. 2.10 on page 149 and Fig. 7.17 on page 313). In general, in oxygen enriched silicon, the built-up of net negative space charge (acceptors) after charged hadron radiation is suppressed. Oxygen catches/binds vacancies. Therefore some cases (EPI, mCZ) do not exhibit "type inversion" after charged hadron irradiation and/or exhibit a donor/acceptor compensating effect (see former sections), clearly violating NIEL. Figure 2.17 shows a clear microscopic to macroscopic correlation: The radiation induced E(30K) concentration in oxygen enriched material is much higher while the H116K, H140K, H152K defect concentration seems unaffected by radiation. E(30K) is an electron trap and a donor (positive space charge) in the upper half of the Si band-gap while the unaffected H complexes are hole traps with acceptor levels (negative space charge) in the lower band-gap; the H complexes are also relevantly responsible for the reverse annealing. Thus the donor E(30 K) is an oxygen-related defect.

Another beneficial side effect is that interstitial oxygen strengthens the lattice and reduces the brittleness of the sensor.

New Materials and NIEL

Obviously, the "old" NIEL mantra is not really adequate any more for the new materials! Charged particles damage differently, protons may even compensate for neutron damage. NIEL is still useful for scaling between different proton energies especially to evaluate the leakage current after hadron irradiation. But, while new

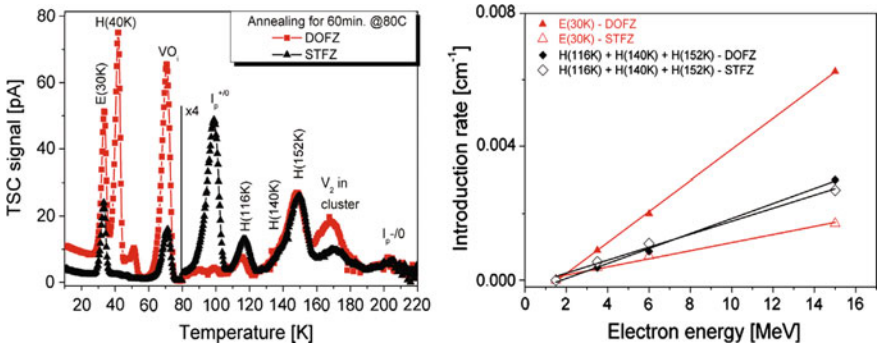

Fig. 2.17 The *left* figure shows the the microscopic defects for standard FZ and diffusion oxygenated Float-Zone DOFZ material determined with the TSC technique; both samples have been irradiated with 6 MeV electrons (creating point and cluster defects). The corresponding introduction rate for E(30K) (donor) and H (acceptor) defects versus electron energy is shown in the *right* plot. Clearly E(30K) introduction (red triangles) is enhanced at high oxygen concentrations while H (black diamonds) is not. More information in [249]

materials seem to be more radiation tolerant, a complete evaluation of each material must be conducted separately for neutron, proton and mixed irradiation. Even the correct radiation mixtures at different radii in the experiment should be checked. Much more complicated and extensive campaigns are necessary to evaluate new materials, processing schemes or companies.

2.2.3 Double Junction

One of the important questions in the last years was: "Does material x,y type-invert or not?". Another question: "Why do we collect charges from considered un-depleted zones in a given device after high radiation?" Is the simple description of a linear field through the full sensor bulk, as depicted in Fig. 1.8 on page 14 still applicable after high irradiation?

Figure 2.18 and earlier Fig. 1.48(lower right) on page 76 show TCT spectra not compatible with a standard assumed linear field across the entire sensor bulk. No clear single slope is visible but a double peak representing fields on both bulk ends with opposite sign. Since the fields are results from space charge, we also expect opposite space charge at the different ends. More examples of the phenomenon will be given, ending with an explanation.

Figure 2.19 depicts the expected linear field configuration after inversion (left) plus a simple two linear field configuration approximating the double junction (middle) and finally the reality parabolic situation determined by simulation and further evaluation of the double peak (right). The lower part of Fig. 2.19 shows the TCT spectra of a 320 μm thick *p*-in-*n* diode after radiation with front side (electron) injection with red laser, plus its derived electric field configuration.

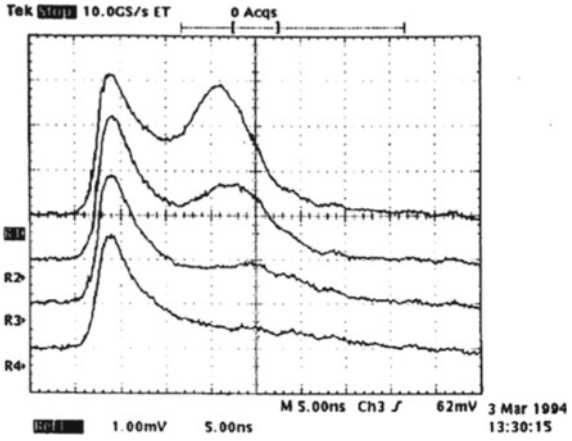

Fig. 2.18 Oscilloscope photo of one of the early reported double peaks in a TCT scan [94]

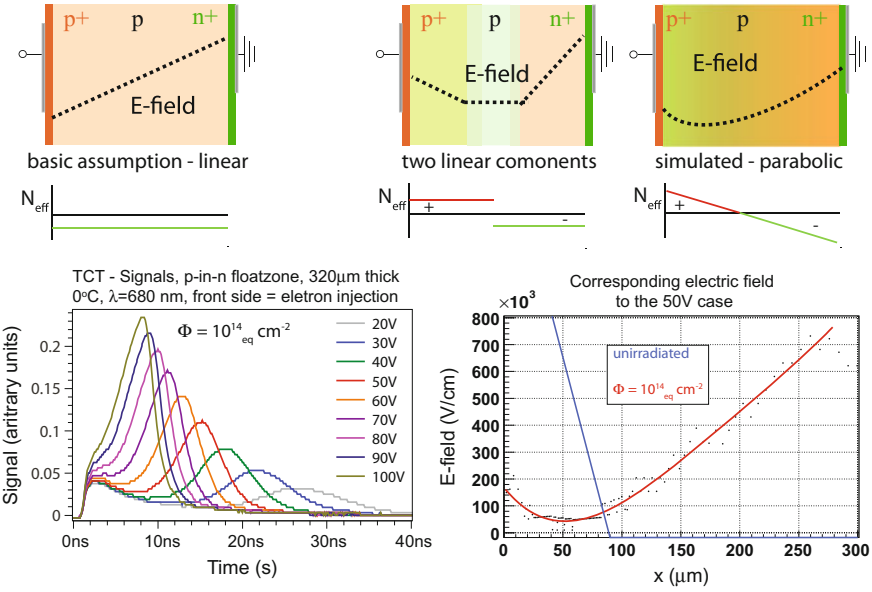

Fig. 2.19 The *left upper* picture depicts the standard linear field expected after radiation – before trapping becomes relevant. The *middle* one shows a double junction described simply by two linear fields and, on the *right*, the parabolic truth derived by simulations. Below the corresponding effective doping concentrations N_{eff} are depicted. The *lower* figure shows the TCT current scans for different voltages; charges are injected by a red laser from the front side (electron injection). The *black dots* on the right show the 'necessary' field to reach the next velocity value of the TCT plot; the *red* represents a simple fit of the points while the *blue* depicts the situation of the corresponding field configuration before radiation [90]

Why do we have a parabolic field after high radiation levels and not the simple expected reversed linear field after type inversion as we have for lower radiation levels? It's another manifestation of bulk current generation centres and, more important, trapping centres in the band-gap. Where is the asymmetry coming from? Defect level concentrations are constant across the entire bulk. But thermally generated charge carriers drift in the electric field to opposite sides (holes travel towards p- and electrons towards n-electrodes) creating an asymmetric but dynamic situation. With the presence of deep level defects, these charges are "trapped", thus "static" and thereby alter the space charge asymmetrically. N_{eff} is no longer uniform leading to a parabolic field across the bulk also described as double junction – distinct junctions at each sensor diode face. N_{eff} corresponds to n (p) doping at the p^+-side (n^+-side).

For values below depletion voltage, the un-depleted zone is located in the middle of the sensor instead of at one end. Still even in the un-depleted zone, fields are present visible in the non-zero current of the TCT and edge-TCT signal (see Figs. 2.19 and 2.21). For $V \gg V_{FD}$ when the field fully reaches through the sensor, one junction, the "main junction", dominates and the field becomes 'more' linear again, the double peak smooths out. After the onset of trapping, the field configuration changes even more with radiation and annealing because it is now defined by three components – intrinsic doping concentration (including radiation defect levels), leakage currents and trapping, all changing with radiation but also with annealing. In addition, charges from ionisation are also trapped thereby altering N_{eff} and thus field configuration. More on the topic in [94, 213]. As for the question about type inversion or no type inversion, often one peak is hidden by trapping thus injecting from one side or the other show a different peak thus a different slope (the one from the visible peak) thus hints to inversion or no inversion depending on the injection side.

The following paragraph shows how the double junction reflects in operation with particles. A CMS n-in-n pixel sensor (DOFZ material) after irradiation beyond the point of type inversion ($\Phi_{eq} = 8 \cdot 10^{14}\ n_{1\mathrm{MeV}}/\mathrm{cm}^2$) is being investigated in a dedicated test beam campaign [65, 88]. The particle beam hits ("grazes") the sensor under a very small angle and thus the traversing particle path in the sensor is very long,

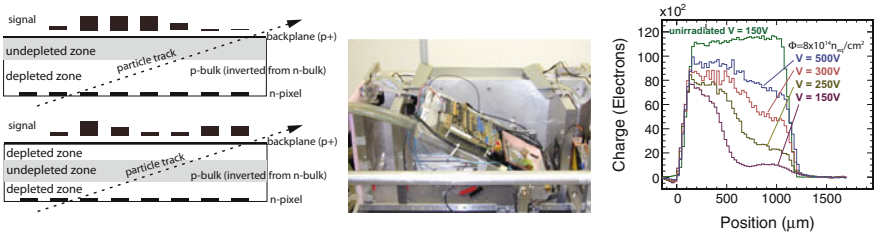

Fig. 2.20 On the *left* we see a cartoon of the incident angle, the position where the ionisation happens and the expected signal distribution. The under-depleted case is depicted for a fully type-inverted case and (*below*) for the double junction case where the un-depleted zone stays in the middle and not at the p^+-face. The expected signal distribution is significantly different. The *middle* photo shows the setup. On the *right*, the data shows a simple flat line for a fully depleted un-irradiated sensor plus the data for under- and fully depleted irradiated sensor given by the different voltages. The data is incompatible with a simple case of type inversion [65, 88]

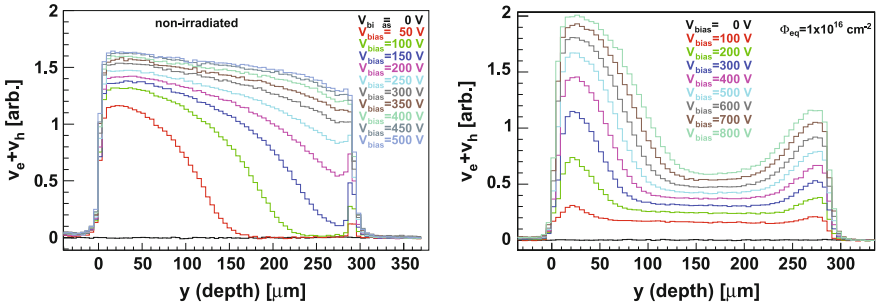

Fig. 2.21 Velocity profiles for different charge injection depths with edge TCT for an un-irradiated and in comparison for a highly irradiated sensor with a double junction. The scans have been done for several voltages mainly all below depletion voltage (which is about $V_{FD} \gg 800\,\mathrm{V}$). The velocity in the middle expectedly un-depleted region is substantially above zero proving an existing electric field. More details and definitely worth to read in [179, 201]

spanning multiple pixels. The z-position corresponds basically to the depth where the ionisation happens; it is called grazing angle method. The cartoon in Fig. 2.20 illustrates simplistically where the charge is created, and the resulted signal distribution expected for a full "type inverted" and one for a double junction configuration (no signal from the un-depleted zones). The measured distribution is incompatible with full "type inversion": (a) charges are collected in the entire volume and (b) the double peak at low voltages indicates high field on both sensor faces and (c) the integrated charge/signal does not scale with the expected depletion depth (with depletion depth $d \sim \sqrt{V}$, $V_B = 300\,\mathrm{V}$ should give $\sqrt{2}$ more signal than $V_B = 150\,\mathrm{V}$). Setup, field configuration and results are complex and only a full simulation sheds light and indicates a parabolic field configuration.

Again, the edge-TCT method (see Sect. 1.8.3 - Edge TCT) demonstrates its strength in Fig. 2.21 investigating the double peak structure injecting charges at certain depths of the sensor and measuring the velocity profile for different voltages – see [178]. The results confirm the above described picture and show a) high fields at both sensor ends but also substantial field strengths in the middle region, even for voltage below V_{FD}. The concept of depletion voltage becomes academic: electric fields are present throughout the sensor and charges are being collected via drift, not random walk. Looking closely, the velocity peak at the back for $V = 500\,\mathrm{V}$, is even larger than the one expected for saturated drift velocities. This hints to charge amplification as described in the next section.

Double junction in a nutshell:

- at high radiation levels with traps present, we have a parabolic instead of a linear field with high but opposite sign maxima at both sensor faces
- the concept of "type inversion" becomes academic
- the concept of V_{FD} becomes academic, since we have field everywhere and therefore directed charge drift everywhere, also below V_{FD}

  - charge collection also from the un-depleted zone

- the different space charge concentrations N_{eff} are due to polarisation, a result from different filling of traps at the different sensor ends (holes/electrons in traps at n/p electrode respectively), due to different drift direction
- the double junction has been proven by standard TCT, grazing angle method in a test beam, and further investigated by edge-TCT. The complex situation is been well described by simulation and simulations are necessary to fully describe, compare and understand the situation
- in the end field strength matters!

2.2.4 *Sensors After Very High Radiation Levels*

With higher fluences, around 10^{16} $n_{1\text{MeV}}/\text{cm}^2$, trapping (trapping time) $\tau_{eff} \sim \Phi_{eq}$ becomes the dominant damage factor, where the electrons and holes, from the ionising traversing particle, are trapped before they reach the readout electrodes. The concept of depletion voltage becomes more and more academic at these fluences. Radiation induced introduction of trap levels differs for the different materials (n, p, FZ, mCz, EPI, oxygenated) but, as reference point, NIEL is applicable for the different radiation types and energies. Substantially large differences exist for electron versus holes collection (n- vs. p-electrode configuration).

Figure 2.22 teaches us that at very high fluences trapping becomes the dominant damage factor (reducing signal) and different particle radiation result in the same effective CCE.

Sensors deployed at the LHC are radiation tolerant up to about 10^{15} $n_{1\text{MeV}}/\text{cm}^2$. The situation gets difficult at fluences of $\sim 5 \cdot 10^{15}$ $n_{1\text{MeV}}/\text{cm}^2$ and above, as foreseen

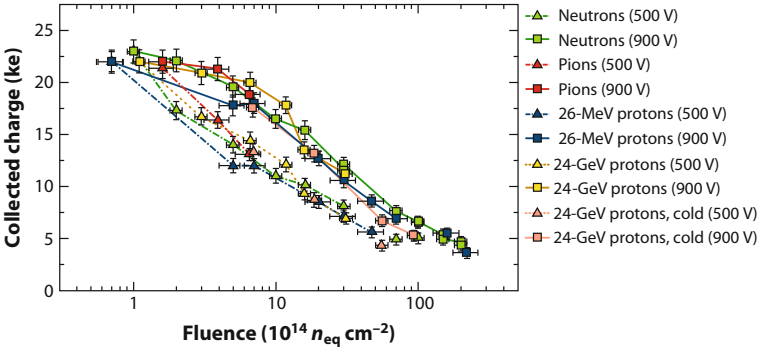

Fig. 2.22 The plot shows CCE for n-in-p FZ strip detectors versus fluence of different particles. At high fluences trapping becomes the dominant factor and damage becomes almost particle independent. The knee in the most right tail looks even a bit too high and could be a hint to charge amplification [11]

for the HL-LHC. New materials and detector schemes had to be developed mainly within RD50 and LHC collaboration efforts (more in Sect. 7.1).

At these fluences, the main relevant question is how much charge is being collected, or better how much charge participates via induction to the signal before being trapped? Adequate signals can be achieved by a combination of the strategies below:

- maximize electric field at the collecting electrode; where the weighting field $\mathbf{E}_W$ is also large
  - if the electric field cannot be established in the full volume; have it at the readout electrode
- establish a geometry with a favourable weighting field
- minimize drift length
- maximize $\mu \cdot \tau_{eff}$ – read electrons

All the above is true for strip/pixel sensors with n-electrode readout either in an n-in-n or n-in-p configuration. After radiation (after SCSI), the depletion zone grows from the n-side and therefore also under-depleted operation is possible differently to p-in-n sensors. n-in-n and n-in-p pixel/strip sensors have a favourable combination of weighting and electric field in heavily irradiated sensors. In reality $\mathbf{E} \cdot \mathbf{E}_W$ after irradiation is much larger for n-in-p compared to p-in-n. Also the collection of electrons seem favourable due to their higher mobility μ and small τ_{eff}; they seem less affected by trapping. For a more detailed discussion the reader is also referred to [173].

The superiority of electron readout is less obvious for pad sensors where electron and holes participate equally to the signal due to the induction process. In general thinner sensors have a higher field but also less volume for the initial ionisation process of the traversing particles and therefore less charges to begin with. This has to be decently balanced. We will see in the next paragraph that field strengths after irradiation can be as large as to amplify the signal. 3D sensors described in Sect. 1.12.7 are reducing drift length by etching narrow electrode columns through the entire sensor volume with spacings much smaller than the sensor thickness.

The baseline choice for the ATLAS and CMS upgrade are n-in-p sensors substantially cheaper than n-in-n ones, which need double-sided processing. Thin n-in-p sensors are even candidates for the innermost radius of the future HL-LHC experiments together with the more special 3D sensors. A drawback of n-electrode readout (n-in-p or n-in-n) sensors is the fact that the high voltage reaches the sensors sides and upper face where additional measures of insulation have to be applied to allow for the readout at GND potential. This is especially true for pixel sensors where the chips are bump bonded directly to the sensors.

More about HL-LHC strategies, plans and R&D in Sect. 7.1.1 where also the annealing behaviour of n-in-p sensors is being discussed.

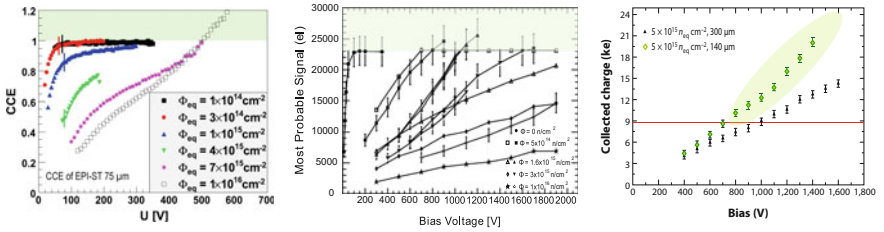

Fig. 2.23 Several groups claim to collect more charge after irradiation than before and even more charge than a MIP deposits in the given material volume. The first plot [188] shows a higher signal in n-EPI material after irradiation, the second [203] a higher signal in p-FZ sensors after neutron irradiation (reactor Ljubljana). The last [59] shows a higher signal in a p-FZ 140 µm thin sensor with respect to the 300 µm thick sensor and also with respect to charge deposited by a MIP in the corresponding volume (after $5 \cdot 10^{15}$ $n_{1\text{MeV}}/\text{cm}^2$ with 25 MeV-p). Clear signatures of charge amplifications have been identified

2.2.5 *Charge Amplification*

Several devices of different material exhibit, after high irradiation, a higher Charge Collection Efficiency than before.

In several cases, more charge per volume has been recorded than the charge deposited by a MIP due to ionisation. Figure 2.23 shows three examples hinting at a charge *amplification* mechanism. It is now of utmost importance to evaluate if the charge amplification is really the wished modus operandi for silicon sensors in the HEP environment. How is the leakage current and the noise affected, what is the resulting effective signal-to-noise? One study shows a correlation of charge collection and leakage current; see Fig. 2.24. The amplification mechanism works for electrons coming from signal as well as from dark current. The impact ionisation comes from the local changes in N_{eff} and the corresponding change/increase in electric field. The situation becomes even more complicated since N_{eff} also changes with annealing and thus the level of amplification can change with time and radiation fluence.

Dedicated investigations with the edge-TCT technique (described in Sect. 1.8.3) are shown in Fig. 2.25. The measurement exhibits a direct indication for charge amplification, the second time-delayed peak in the current pulse can be explained by electron–hole creation at the very high electric field at the strip face. The effect is very similar to gas wire detectors, where ions from the primary ionisation are registered early while a larger ion signal from the secondary avalanche ionisation within the high field region near the wires is recorded much later. The corresponding holes from the amplification process have been excited later than the original ones from light injection and then drift from the strip region to the backside. A second observation by this method, not detailed here, is that the velocity and electric field profiles do not give a consistent picture without charge amplification (more in [178]).

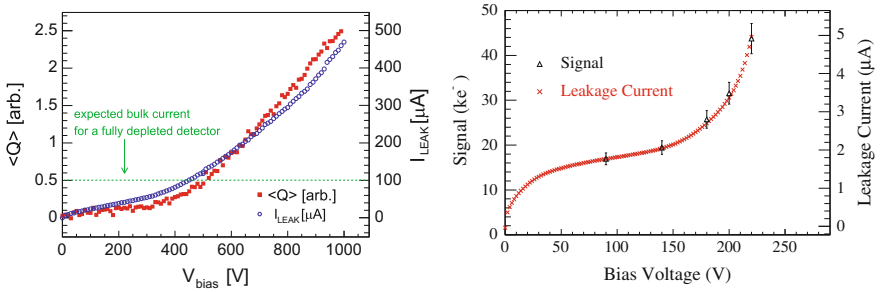

Fig. 2.24 Collected charge versus leakage current in the regime of amplification. Two examples indicating that charges generated by traversing particles as well as the thermally generated charges that constitute the leakage current are multiplied by the same factor once the field is high enough for avalanche multiplication. The *left* [178] is a measurement on a planar sensor, the *right* [230] on a 3D sensor

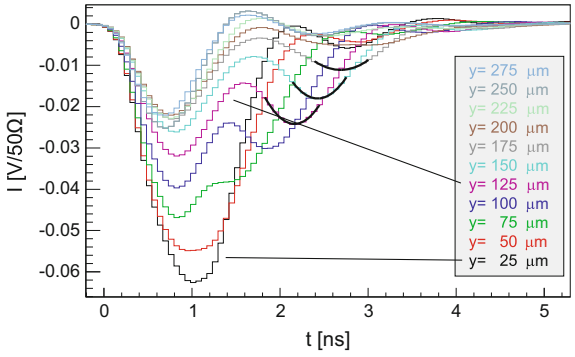

Fig. 2.25 The second peak in the hole tail is evidence of charge amplification in n-in-p sensors in the high E-field strip region. The first peak corresponds to charge carriers from the initial laser light, the additional peak in the tail represents additional holes created at a later time together with electrons in the amplification process when the electrons reach the high field strip region; the holes then need to drift to the back [178]

In the end S/N, efficiency, resolution and power consumptions are the important parameters. Dedicated designs might be able to make use of the amplification feature. Inspired by the amplification, in the framework of RD50 dedicated structures are being designed and produced, namely **L**ow **G**ain **A**valanche **D**etectors LGAD [56, 232, 233, 262] – more in Sect. 1.12.8. LGAD represents a new concept of silicon radiation detector with intrinsic multiplication of the charge. These new devices are based on the standard Avalanche Photo Diodes APD, normally used for optical and X-ray detection applications, but they give a low gain, suitable for detecting high energy charged particles, and allow fine segmentation pitches.

Another aspect of amplification sensors is the increase in speed/slew rate and they open the possibility for fast timing [263]. CMS is exploring to use LGADs as a timing layer in the forward direction in front of the future high granularity calorimeter for the HL-LHC and they are candidates for ATLAS/CMS very forward detectors.

2.3 Surface Damage

The term surface damage describes all radiation-induced damages in the SiO_2 layer and in the SiO_2–Si interface. This effect is therefore prominent in AC-coupled sensors and in the NMOS and PMOS transistors of all kinds of electronics.

The damage is introduced by ionisation and not atomic displacement, unlike in the silicon bulk damage described earlier. In contrast to the situation in the silicon bulk, creation of electron–hole pairs is not fully reversible in an insulator. Depending on the oxide quality, recombination varies between several percent and almost 100%. In addition to recombination, generated charge carriers can also be captured by existing defects, where the emission is highly suppressed, since the band gap is much larger in oxide and nitride layers ($E_g = 8.8$ eV in SiO_2 and $E_g = 5$ eV in Si_3N_4). In the oxide, the mobility of electrons ($\mu_{e,SiO_2} \approx 20\ \frac{\text{cm}^2}{\text{Vs}}$) is several orders of magnitude higher in the oxide than that of holes ($\mu_{h,SiO_2} \approx 2 \cdot 10^{-5}\ \frac{\text{cm}^2}{\text{Vs}}$). This leads to a fast separation of electron–hole pairs. Electrons drift to the metal electrode, while the holes drift by a hopping mechanism via shallow levels to the Si – SiO_2 interface, especially when a voltage is applied (Fig. 2.26). The effect is enhanced for a positive voltage applied on the metal side during radiation; electron movement is accelerated to the metal side and holes drift to the interface, a standard mode for a transistor. In addition the defect concentration is especially high at the interface due to lattice mismatch and dangling bonds. The trap density in the interface region is around 10^9 – 10^{10} traps/cm^2. As a result, positive static charges accumulate at the interface, saturating at about $N_{ox} \approx 3 \cdot 10^{12}$ cm^{-2} [358]. The introduced additional oxide volume and interface charge concentration is now increasing the flat-band voltage by

$$\Delta V_{flat} = -\frac{1}{\varepsilon_{ox}\varepsilon_0}\left(\sigma_{int} d_{ox} + \int_0^{d_{ox}} \varrho(x) x dx\right) \tag{2.21}$$

where d_{ox} is the oxide thickness, σ_{int} is the surface charge at the Si – SiO_2 interface and $\varrho(x)$ reflects the introduced additional charge density in the oxide volume.

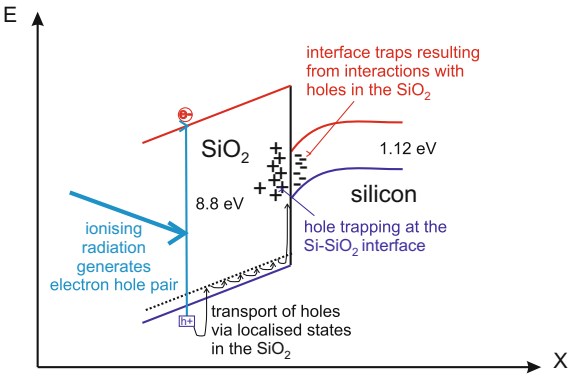

Fig. 2.26 Radiation damage in the Si – SiO_2 Interface

Therefore, measuring the flat-band voltage changes is a diagnostic tool to investigate surface damage. Negative charges are now attracted from the bulk side towards the interface and accumulate there, decreasing the inter-strip resistance and increasing polarisability, thus capacitance. For thick oxides, with a large enough positive oxide charge the 'surface depletion' can switch to 'electron accumulation', decreasing inter-strip resistance. As a second step also negative traps are attracted towards the interface from the bulk side. Figure 2.27 displays the field configuration without and with high oxide charge concentration. Section 6.4.2 describes how the use of <100> silicon minimizes the effect by reducing the number of dangling bonds.

To summarize, due to ionisation, insufficient recombination and subsequent trapping of holes at the Si – SiO_2 interface, the following macroscopic results deteriorate the sensor functionality.

- increase of inter-strip capacitance, thus increasing noise
- decrease of inter-strip resistance, thus increasing cross-talk
- increase of flat-band voltage, as an indicator for oxide charge.

A small annealing effect at high temperatures ($T \gg RT$; around 100 – 400 °C) is also observed here, explained by the drift of bulk electrons into the near-interface region and recombination with holes trapped there. Unfortunately the reverse annealing effects at these temperatures do not allow to benefit from surface damage annealing.

While the damage mechanism in electronic circuits is the same as for the MOS structure in AC-coupled sensors, the static charge centres have several additional effects for NMOS and PMOS. Figure 2.28 shows the basic schema. The main effects are

- threshold voltage shift of transistor V_{thr}
- increased noise
- increased leakage current.

The main drawback of radiation damage in electronics is the increase of transistor threshold voltage V_{thr} and leakage current. The increased threshold voltage derives

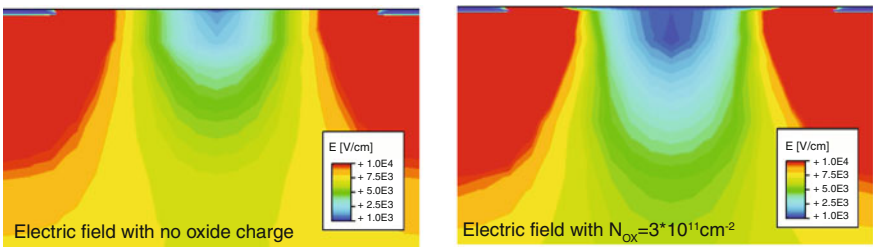

Fig. 2.27 Inter-strip region fields with/without oxide charges. The additional charges do disturb the field distribution. The low-field region in the intermediate region of the strips (*right picture*) allows for negative charge carriers. These are increasing polarisability and thus capacitance and are decreasing the strip-by-strip insulation, which is completely defined by the field distribution [79]

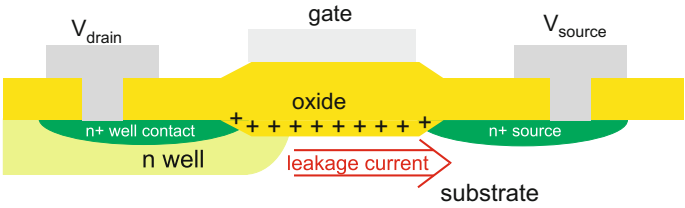

Fig. 2.28 Scheme of an NMOS transistor with deteriorating oxide charge from radiation. The oxide charge screens the gate voltage and therefore a higher threshold voltage V_{thr} is needed to operate the transistor. The resulting attracted charge carriers in the substrate region increase leakage current. The accumulating negative traps in the substrate finally affect mobility. Resulting energy levels in the mid-band region also reduce lifetime and therefore increase leakage current

from the screening effect of the oxide charge concentration. The shift of V_{thr} is proportional to a power n of the oxide thickness d_{ox} : $V_{thr} \propto d_{ox}^{n}$. The power factor n depends on the processes used to grow the oxide and its thickness. It has been measured to be in the range of 1 – 3. The increase of leakage current is induced by the traps acting as a mid-bandgap level introducing recombination centres, thus decreasing lifetime and therefore increasing leakage current. In addition the static traps in the interface affect the mobility in the conducting case. Finally, the accumulation of positive charges in the oxide, especially in thick oxides, can form parasitic charge transfer paths in the substrate by creating inversion layers between N-wells in the substrate. This can lead to a decrease in the signal-to-noise ratio or even to short circuits in the transistor. In the case of NMOS transistors, the charge-up of the oxide may reach a concentration that makes it impossible to completely switch off the transistor.

In Sect. 6.4.1 on page 239 the enclosed transistor design together with the deep sub-micron processing is described which is the key technology for radiation-tolerant electronics.